

Transient Dynamics of a Miura-Origami Tube during Free Deployment

Haiping Wu,¹ Hongbin Fang^{2,3,4,*}, Lifan Chen,¹ and Jian Xu^{2,3,4}

¹*Department of Aeronautics and Astronautics, Fudan University, Shanghai 200433, China*

²*Institute of AI and Robotics, Fudan University, Shanghai 200433, China*

³*Engineering Research Center of AI & Robotics, Ministry of Education, Fudan University, Shanghai 20043, China*

⁴*Shanghai Engineering Research Center of AI & Robotics, Fudan University, Shanghai 200433, China*

 (Received 15 May 2020; revised 2 August 2020; accepted 25 August 2020; published 29 September 2020)

With excellent folding-induced deformability and shape reconfigurability, origami-based designs have shown great potential in developing deployable structures. Noting that origami deployment is essentially a dynamic process, while its dynamic behavior remains largely unexplored, owing to challenges in modeling. This research aims to advance the state of the art of origami deployable structures by exploring the transient dynamics under free deployment, with the Miura-origami tube being selected as the object of study because it possesses a relatively simple geometry, exceptional kinematic properties, and a wide range of potential applications. In detail, a preliminary free-deployment test is performed, which indicates that transient oscillations in the transverse direction are non-negligible, and tube deployment is no longer a single degree of freedom mechanism. Based on experimental observations, four assumptions are made for modeling purposes, and a $2N$ degree of freedom dynamic model is established for an N -cell Miura-origami tube to predict the transient oscillations in both deploying and transverse directions. Employing the settling times and the overshoot values as transient dynamic indexes, a comprehensive parameter study is then carried out. It reveals that both the physical and geometrical parameters will significantly affect the transient deploying dynamics, with some of the parameter dependence relationships being counterintuitive. The results show that the relationships between the transient dynamic behaviors and examined parameters are sometimes contradictory in the deploying and transverse directions, suggesting the necessity of a compromise in design. Overall, this research proposes a systematic method for constructing an origami dynamic model. Although only the Miura-origami tube is exemplified in detail, the methodologies are promising for application to other origami deployable systems because the established model is believed to be able to capture the essential characteristics of origami deployment, and meanwhile, hold good processability. In addition, comprehensive parameter analysis results could provide useful guidance for the design and optimization of Miura-origami deployable tubes with robust dynamic performance.

DOI: [10.1103/PhysRevApplied.14.034068](https://doi.org/10.1103/PhysRevApplied.14.034068)

I. INTRODUCTION

Generally, a deployable structure is defined as a structure that can transform between different shapes, so as to significantly change its size [1]. In the space industry, using the concept of deploying is an appealing solution to overcome the strict constraints set by launch-vehicle fairing sizes. Typical space-deployable structures include solar panels, antennas, booms, and masts. [2]. The scope of deployable structures is not confined to space applications, they have also been applied in biomedical sciences, architectures, optics, and robotics [1,3,4].

Recently, origami, the art of paper folding, has been recognized as a novel platform for developing deployable structures. While originating from art, currently, origami

inclusively indicates all folding practices that transform two-dimensional crease patterns into three-dimensional shapes, regardless of the materials that are used. Origami structures are proven to possess unique advantages, including infinite design space, excellent deformability and shape reconfigurability, flat foldability, a single degree of freedom (SDOF) folding mechanism, and extraordinary folding-induced kinematic and mechanical properties. With these merits, origami opens up alternative possibilities for developing deployable structures. On one hand, the origami principle is utilized to interpret the underlying mechanism of natural deploying phenomena, especially in the plant kingdom [5–7]. On the other hand, origami-based designs are exploited for various deployable structures in a variety of fields [8–11], including self-deployable stent grafts [12], foldable robots [13–16], acoustic and optical devices [17–19], architectural structures [3,20,21], and

* fanghongbin@fudan.edu.cn

mechanical metamaterials [22–24]. Particularly, origami finds value in deployable space structures [10]. In 1985, Miura proposed a flat-foldable and rigid-foldable origami pattern, namely, the Miura-origami (for short, Miura-ori) pattern, for compactly folding solar sails and panels [25]. It is revealed that folding of the Miura-ori pattern is a SDOF mechanism with a noteworthy negative Poisson's ratio [26]. Hence, since its birth, the Miura-ori, and its close relatives, has become the most popular fold pattern for origami-inspired space structures [27–29]. In addition to the Miura-ori, other fold patterns that can be used for deployable space structures include the flasher patterns [30–32]; the Yoshimura patterns [33]; the Kresling patterns [34,35]; the curved crease patterns [36]; as well as various foldable cylinders, tubes, and cones [35,37,38].

With the upsurge of deep-space detection and manned space missions, there is a higher request for the precision and reliability of large-scale deployable structures. Conventional research efforts that focus only on the stowed and deployed configurations would be insufficient, and there is a necessity to consider the dynamics of deployment. However, the current research level on the transient dynamics of deployable structures lags far behind the other extensively addressed areas (including the geometric and kinematic properties [39], structural analysis of stowed and deployed configurations [40], and packaging and folding techniques [25]). Part of the reason is that the deployable structure is designed for the space environment, so ground testing is often not a feasible option, owing to the excessive size and gravity environment. Thus, the prediction of the on-orbit deploying performance heavily relies on dynamic modeling of the system. However, an accurate and processable model is always difficult to establish, because a deployable structure generally consists of numerous rigid and flexible components that are coupled together, and the physical parameters are partly unknown or difficult to measure. McPherson and Kauffman provide a systematic review of the current work on space-deployable structure dynamics [41].

For origami structures, crease pattern designs, folding kinematics, quasistatic properties, and actuation methods are the main areas of concern that are well derived in the literature [8,9,11,24,42]. Notably, in practice, the origami structures may suffer from external excitation, and folding can be a dynamic process; however, origami dynamics research is still in its infancy. One way to build the dynamic model is to simplify the origami structure into an equivalent truss structure [43–45]. Based on this concept, nonlinear wave dynamics of Tachi-Miura polyhedron and triangulated cylindrical origami metamaterials are explored [43,44]. Another way to derive the equation of motion is to consider the origami structure as a highly nonlinear spring [46–50], the equivalent constitutive relation of which can be obtained by energetic approaches or quasistatic tension and compression tests.

For the sake of analysis, the constitutive relation can be further approximated by polynomials. Based on this idea, Fang *et al.* uncovered that the intrinsic bistability of the stacked Miura-ori (SMO) cell could induce complex dynamic behavior, as verified by a systematic experimental investigation [46]. In addition to these two methods, pure experimental or simulation studies on the dynamics of origami structures have also been reported [51–53], which provide a direct understanding of the dynamic behavior of origami structures.

The abovementioned pioneering research into origami dynamics has been limited to steady-state responses (e.g., wave propagations [43,44,47] or forced oscillations [46, 48,54]). For origami deployable structures, the transient deploying dynamics is of greater significance in determining the performance, which, however, is not well understood. On one hand, the transient dynamics is likely to depend strongly on the physical properties and complex nonlinear geometries of the origami deployable structures. Analyzing such dependency relationships calls for accurate dynamic modeling; nonetheless, there is a lack of mature origami dynamic modeling methodology. On the other hand, in practice, rigid folding of the origami structure cannot be perfectly ensured, which may thus break the SDOF assumption and induce multiple degrees of freedom (MDOF) motion. Although motions other than folding are always ignorable in quasistatic folding, neglecting them in transient dynamic analyses may cause serious consequences, especially for origami space-deployable structures working in orbit.

Based on the above statement, this research aims to advance the state of the art by solving two problems. First, is it possible to establish an accurate and processable model for predicting the transient dynamics of a practical origami deployable structure? The two modeling techniques mentioned above, i.e., the equivalent truss [43–45] and the equivalent nonlinear spring [46–50] representations, accomplish the first step by simplifying the complex origami structure into an analyzable dynamic system. However, admittedly, some key attributes of origami structures are missing in the simplification, such as the inertia of origami facets; some important characteristics of folding cannot be captured by these oversimplified models, such as the additional DOF induced by nonideal creases. Putting these factors into consideration calls for an entirely different modeling approach. Second, what are the qualitative and quantitative relationships between the transient dynamic performance and the structural parameters? Answering this question requires a systematic examination of the transient dynamics and a comprehensive parameter study, which, ultimately, could offer insights and guidance for the development of origami deployable structures with robust dynamic performance.

To address these research goals, the Miura-ori tube is selected as the object of study and its free deployment

is focused upon. The reasons for choosing the Miura-ori tube are threefold. First, tubelike origami structures could support loads, while exhibiting large folding deformations. They have wide applications in structures that call for uniaxial extensions, such as deployable space booms and masts [10,33,37,55]. Second, the Miura-ori tube possesses the simplest geometry for analysis; its constituent unit is a degree-four vertex cell with inherent reflectional symmetry and collinear creases. In an ideal case, the Miura-ori tube is rigidly foldable with a SDOF mechanism. Although other origami tubes made of Yoshimura and Kresling patterns can exhibit richer deformations [10,45,55], they are no longer rigidly foldable, which would introduce additional complexities to the dynamic modeling and prototype fabrication. Third, practically, the rigid-foldability and SDOF folding mechanism of the Miura-ori tube may be partly broken. Hence, the Miura-ori tube could serve as a good platform for studying the transient dynamics in both the uniaxial deploying direction and the transverse direction. It is worth noting here that the aim of this research is to break through the bottleneck in transient dynamic modeling and parameter dependence relationship, as exemplified by the Miura-ori tube, rather than putting forward an alternative deployable structure design. Nevertheless, the proposed modeling technique and the developed dynamic analysis method are promising for application to other nonsoft origami deployable structures.

The rest of this paper is organized as follows. Section II introduces the kinematic model of the Miura-ori tube and demonstrates the results of a preliminary free-deployment test. Insights from the preliminary experiment could provide useful hints for dynamic modeling and analysis. Section III details the dynamic modeling technique, including modeling assumptions and the equation of motion. Based on this, a comprehensive parameter study is carried out in Sec. IV. The effects of the physical and geometric parameters on deploying dynamic performance, as characterized by the settling times and overshoot values, are provided and interpreted. A summary and conclusions of this research, as well as a heuristic discussion, are presented in Sec. V.

II. RIGID-FOLDING KINEMATICS AND PRELIMINARY EXPERIMENTS

In this section, rigid-folding kinematics of the Miura-ori tube is first introduced. Then, a six-cell prototype is fabricated, and a preliminary free-deployment test is carried out to gain insights into the fundamental characteristics of the transient dynamics.

A. Rigid-folding kinematics of the stacked Miura-ori cell

Figure 1(a) shows a Miura-ori tube consisting of six SMO cells; each SMO cell is stacked by two Miura-ori

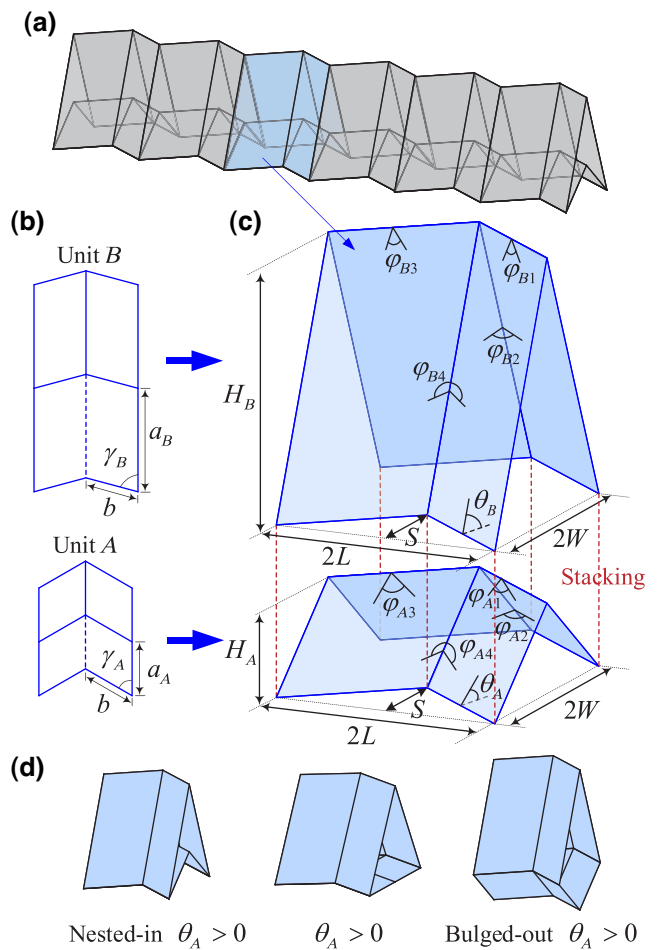


FIG. 1. Geometries of the stacked Miura-ori cell. (a) Miura-ori tube (in the nested-in configuration) composed of six identical SMO cells, where a constituent cell is highlighted. (b) Planar crease patterns of constituent Miura-ori units *A* and *B*, where the internal solid and dashed lines indicate the “mountain” and “valley” creases, respectively. (c) SMO cell in a magnified view; the dihedral angles $[\varphi_{ki} (k = A, B; i = 1, 2, 3, 4)]$ between adjacent facets, folding angles $(\theta_A$ and $\theta_B)$, and external dimensions $(2L, 2W, H_A, H_B$ and $S)$ are indicated. (d) SMO cell at the nested-in configuration $(\theta_A > 0)$, intermediate configuration $(\theta_A = 0)$, and bulged-out configuration $(\theta_A < 0)$.

units with kinematic constraints [Fig. 1(b)]. In detail, the geometries of a Miura-ori unit can be characterized by three parameters, namely, the lengths of two adjacent crease lines, a_k and b_k , and the sector angle γ_k between them, where $k = A, B$, denoting bottom unit *A* and top unit *B*, respectively. Without loss of generality, bottom unit *A* is assumed to have the shorter crease length, i.e., $a_A < a_B$. With the rigid-origami assumption, folding of the Miura-ori unit is a SDOF mechanism, which can be described by the folding angle $\theta_k (k = A, B)$, defined as the dihedral angle between the facet and reference *x-y* plane [Fig. 1(c)]. To ensure kinematic compatibility between the two

units, so that they remain connected during the whole folding process, the following constraints have to be satisfied [26,56]

$$b_A = b_B = b, \quad a_A \cos \gamma_A = a_B \cos \gamma_B. \quad (1)$$

When stacked together, folding of the two units is no longer independent of each other; rather, the folding angles θ_k ($k = A, B$) are constrained by

$$\cos \theta_A \tan \gamma_A = \cos \theta_B \tan \gamma_B. \quad (2)$$

Equation (2) indicates a nonunique relation between folding angles θ_A and θ_B . When $\theta_A \in [-\pi/2, \pi/2]$, θ_B remains non-negative; in other words, for a given positive value of θ_B , θ_A could take two values with the same magnitude, but opposite signs. In what follows, θ_A is employed to describe the folded configuration of the SMO cell. When $\theta_A > 0$, bottom unit A nests into top unit B , and the configuration is referred to as “nested-in;” when $\theta_A < 0$, bottom unit A bulges out of top unit B , and the configuration is referred to as “bulged-out” [Fig. 1(d)]. By properly prescribing the geometric design and crease stiffness, the SMO cell would be equipped with bistability, possessing a nested-in and a bulged-out stable configuration [Fig. 1(d)]. Transitions between these two stable states call for actuation forces along the height direction [46], internal pressure [57], or dynamic excitations [46].

The folded configuration of a Miura-ori unit can also be characterized by the dihedral angles between adjacent facets φ_{ki} ($k = A, B$; $i = 1, 2, 3, 4$) [Fig. 1(c)], which are functions of the folding angles θ_k . Based on spherical trigonometry, we have [46]

$$\sin \frac{\varphi_{k2}}{2} = \frac{\cos \theta_k}{\sqrt{1 - \sin^2 \theta_k \sin^2 \gamma_k}}, \quad (3)$$

$$\varphi_{k1} = \varphi_{k3} = \pi - 2\theta_k, \quad \varphi_{k4} = 2\pi - \varphi_{k2}.$$

Here, for the nested-in configuration ($\theta_A > 0$), we assign $\varphi_{A2} \in (0, \pi)$; and for the bulged-out configuration ($\theta_A < 0$), we assign $\varphi_{A2} \in (\pi, 2\pi)$. At the connecting creases between the two constituent Miura-ori units, the dihedral angle is

$$\varphi_C = \theta_B - \theta_A. \quad (4)$$

Based on the above geometry analysis, the external dimensions of an SMO cell can be derived [26] by

$$L = \frac{b \sin \gamma_A \cos \theta_A}{\sqrt{1 - \sin^2 \theta_A \sin^2 \gamma_A}}, \quad W = a_A \sqrt{1 - \sin^2 \theta_A \sin^2 \gamma_A} \\ S = \frac{b \cos \gamma_A}{\sqrt{1 - \sin^2 \theta_A \sin^2 \gamma_A}}, \quad H_k = a_k \sin \theta_k \sin \gamma_k \quad (k = A, B). \quad (5)$$

TABLE I. Geometries of the Miura-ori tube prototype.

a_A (mm)	a_B (mm)	b (mm)	γ_A (deg)	γ_B (deg)
38.1	73.6	38.1	60	75

B. Prototype design and fabrication

To gain a basic understanding of the transient dynamic behavior of the Miura-ori tube during free deployment, preliminary experiments are carried out. To this end, a Miura-ori tube is prototyped, with the geometry parameters listed in Table I. The fabrication procedures are demonstrated in Fig. 2. In detail, the origami facets are laser cut individually from 0.25-mm-thick stainless-steel sheets, and 0.1-mm-thick adhesive-backed plastic films (ultrahigh molecular weight polyethylene) are used to connect the facets into two separate six-cell Miura-ori sheets [top sheet and bottom sheet, Fig. 2(a)]. To assign the origami structure with appropriate folding stiffness, based on our past experiences [46], three 0.1-mm-thick prebent spring-steel stripes are pasted at the creases with length a_B in the top Miura-ori sheet [Fig. 2(b)]. The prebent angle of the spring-steel stripes is about 85.3° , corresponding to a stress-free configuration of the SMO structure with $\theta_A^0 = 60^\circ$. Then, the top sheet and the bottom sheet are stacked and connected via adhesive-backed plastic films, generating a six-cell tube prototype. Figure 2(c) shows photographs of the prototype (in the nested-in configuration) from two different angles of view. Considering that the constituent SMO cell is mirror-symmetric, the tube is fundamentally made up of 12 half SMO cells (“half-cell” for short in what follows). A single half-cell is indicated in Fig. 2(c) by a dashed rectangle.

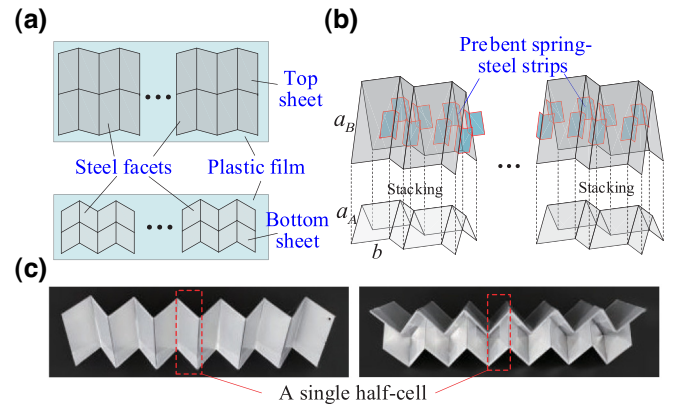


FIG. 2. Fabrication of the Miura-ori tube prototypes. (a) Connecting laser-cut steel facets into top and bottom Miura-ori sheets via adhesive-backed plastic film. (b) Stacking the top sheet and bottom sheet into a tube. Prebent spring-steel stripes are pasted at the creases with length a_B . (c) Photographs of the six-cell prototype (in the nested-in configuration) from two angles of view, where a single half-cell is indicated.

C. Setup for free-deployment test

Figures 3(a) and 3(b) show a sketch and photograph of the experimental setup. The Miura-ori tube prototype (in the nested-in configuration) is fixed to a customized acrylic panel at one end via foldable steel sheets and movable screw rods [Fig. 3(c)]. In detail, on the acrylic panel, a groove and two sliding chutes are designed based on the rigid-folding kinematic of the SMO cell [Fig. 3(d)]. At point H_1 , a pair of foldable steel sheets are used to connect the prototype with the panel, with one sheet inserted into the panel through the groove, and the other sheet connected with the prototype at the crease via adhesive-backed plastic film. At points H_2 and H_3 , screw rods are utilized to connect the prototype with the panel. For each screw rod, one end is fixed with the prototype along the crease via adhesive-backed plastic films, and the other end is free to move along the sliding chute. The chute trajectory corresponding to points H_2 and H_3 is an arc and a horizontal line segment, respectively; they are determined based on

$$|\overline{H_1H_3}| = a_B, |\overline{H_2H_3}| = a_B, |\overline{H_1H_2}| = 2W, \quad (6)$$

where W is derived in Eq. (5). Based on the above setup, folding of the related facets is not affected. However, the displacements of point H_1 in all directions are completely constrained; points H_2 and H_3 are allowed only to move along the chutes. For easy descriptions, a global Cartesian coordinate system is set with the origin located at point H_1 , the x axis pointing along the deploying direction, and the y axis pointing along H_1H_2 . Hence, we have $x_{H_1} = y_{H_1} = z_{H_1} = 0$, $x_{H_2} = 0$, $z_{H_2} = 0$, and $x_{H_3} = 0$.

To examine the displacements of the constituent SMO cells in the x , y , and z directions, 6 markers (denoted by F_1 to F_6) are pasted at the outermost vertices in the front of the prototype; and another 12 markers (denoted by T_1 to T_6 , and T_{1b} to T_{6b}) are pasted at the top vertices of the prototype [Fig. 3(a)]. In the experiments, the tube prototype first stays at a precompressed configuration with the help of a string for fixing. The free end of the tube is suspended from the ceiling by a light string to reduce the effects of gravity. By setting a fire and burning through the string, the compressed prototype is released to perform a free deployment. Two high-speed cameras (Phantom® VEO 640), with one arranged on the top of the prototype, and the other arranged in front of the prototype, are used to record the displacements of the markers [Figs. 3(a) and 3(b)]. In detail, displacements of the constituent cells in the x and y directions can be read from markers T_1 to T_6 via the top camera; displacements in the z direction can be read from markers F_1 to F_6 via the front camera. The sampling rate of the cameras is set to be 1000 fps (frames per second).

D. Preliminary experimental results and understandings

Based on the abovementioned setup, free-deployment tests are carried out on the prototype. The high-speed camera record frames for no less than 6 s. Figure 3(e) displays the images obtained from the high-speed cameras at six key time instants, namely, the initial instant (0 ms), the instant when the string is burnt through (160 ms), the first time when the tube is deployed to the largest length (242 ms), the instant when the tube exhibits the largest displacement in the negative y direction (552 ms), the instant when the tube exhibits the largest displacement in the positive y direction (1020 ms), and the final instant when the cameras stop recording (6000 ms). Figure 4 displays the measured displacement-time histories of the six constituent SMO cells in the x , y , and z directions. The following phenomena are observed and interpreted.

(i) During free deployment, rigid-folding kinematics of each half-cell is basically satisfied within each half-cell. However, folding of all constituent half-cells shows significant discrepancies, which can be clearly observed in the frames at 160 ms in Fig. 3(e).

(ii) In addition to the expected transient vibrations along the deploying direction (i.e., the x direction), the tube exhibits significant transverse vibrations in the y direction. Transverse vibrations in the z direction are also detected; however, overall, the vibration amplitudes are much lower than those in the y direction.

(iii) In the x , y , and z directions, the transient vibrations of the constituent cells are synchronized, in general, exhibiting conspicuous characteristics of underdamped vibrations. However, their vibration amplitudes are distinctly different. The farther away from the fixed end, the larger the amplitude is. Particularly, the cell at the free end [measured from markers T_6 and F_6 , Figs. 4(a)–4(c)] always exhibits the largest vibration amplitudes. To have a clear comparison, the corresponding displacement-time histories are extracted and displayed in Fig. 4(d).

(iv) Focusing on the cell at the free end (characterized by markers T_6 and F_6), we notice that the transient vibration amplitude in the y direction is much more significant than that in the z direction. During the initial releasing stage (within 800 ms), due to the imperfect precompressed configuration and the nonideal fixed-end connection, the vibration is relatively irregular, with the largest peak-peak amplitude being 40.82 mm in the y direction and 26.45 mm in the z direction. After that, the oscillation in the z direction decays fast; around 1000 ms, the largest peak-peak amplitude is only 2.63 mm in the z direction, which is about 7.6 times lower than that in the y direction (22.62 mm).

Notably, if, with the rigid-folding assumption, folding of the whole Miura-ori tube is a SDOF mechanism,

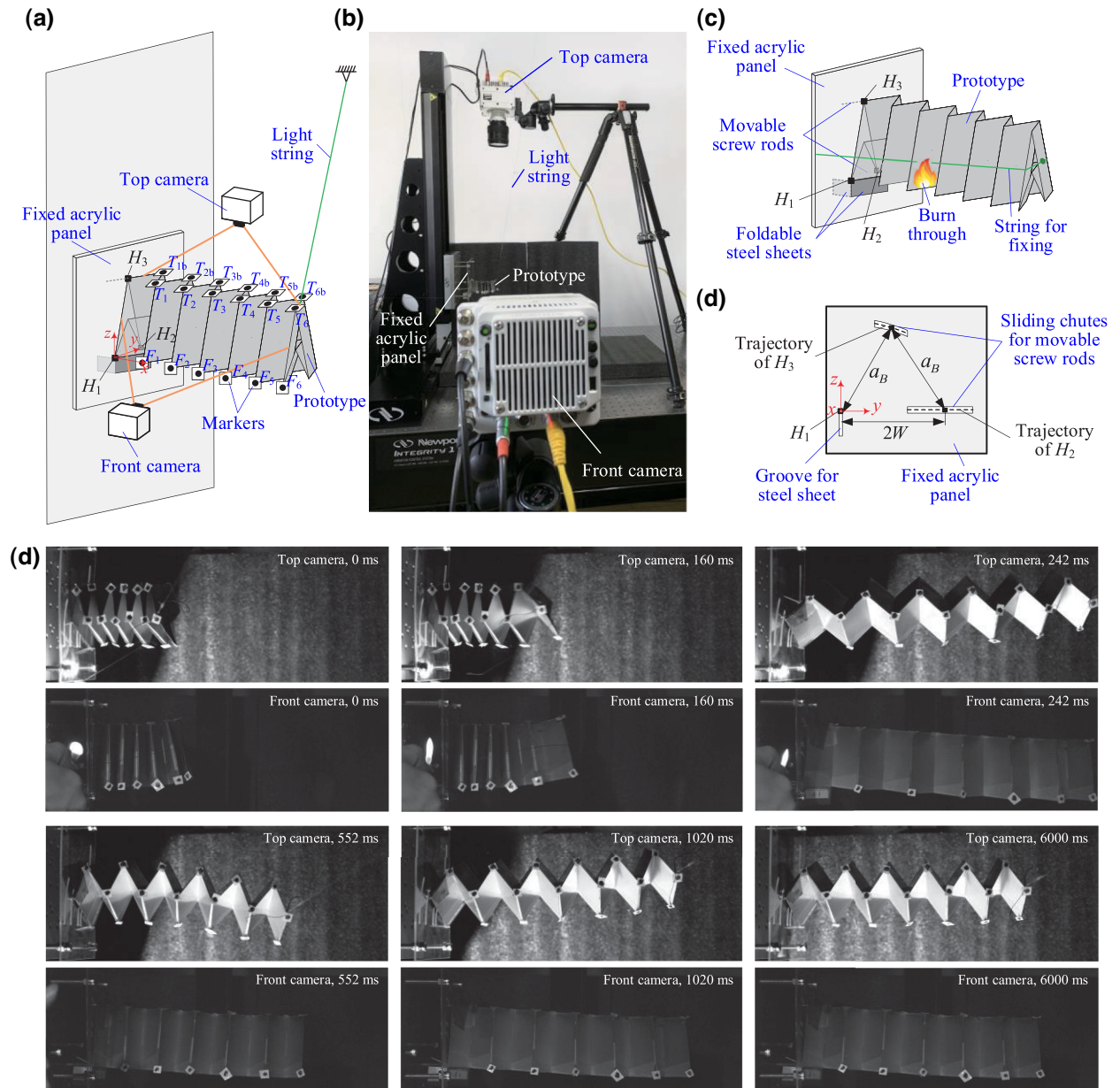


FIG. 3. Preliminary experiment on the free deployment of a six-cell Miura-ori tube. (a) Sketch and (b) photograph of the experimental setup. Displacements of the markers on the prototype are measured by top and front high-speed cameras.

transverse displacements of the tube cannot occur. However, in our experiment, significant transverse vibrations in the y direction are observed. This is because, in a real tube prototype, the creases made in plastic films cannot be considered as ideal torsional hinges anymore; rather, they would exhibit non-negligible deformations, inducing torsional deviations between adjacent facets. Under the circumstances, a SDOF rigid-folding dynamic model is insufficient to predict the transient dynamic behavior of a real origami tube, and it becomes a necessity to set up an improved dynamic model by considering the nonideal creases.

III. DYNAMIC MODELING

Fundamentally, the Miura-ori tube is a rigid-flexible coupled system and establishing its dynamic model is generally a challenging task. Fortunately, the preliminary free-deployment test provides some useful hints to simplify the dynamic modeling.

A. Model assumptions

A generic N -cell Miura-ori tube consists of $2N$ half-cells. For ease of descriptions, “ i, j ” is used to denote each vertex. The first number i indicates the i th half-cell

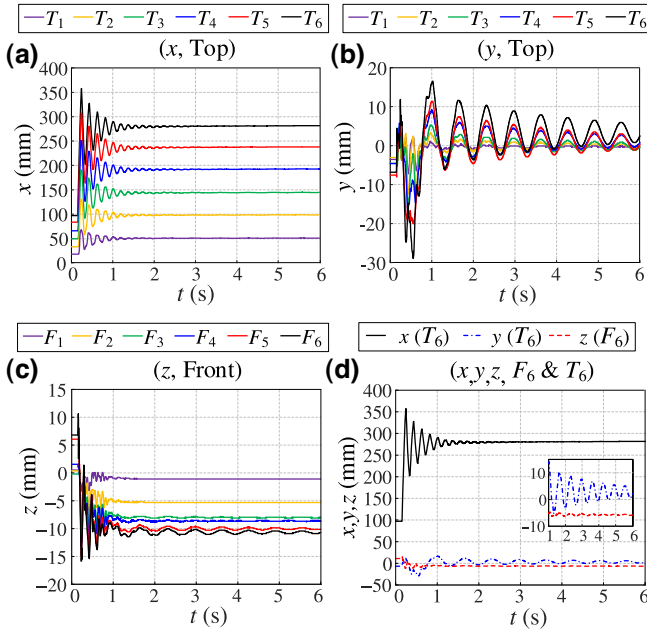


FIG. 4. Transient response of the Miura-ori tube prototype in a free-deployment test, as recorded by high-speed cameras. (a)–(c) Displacement-time histories of the constituent cells in the x , y , and z directions, respectively [measured from markers T_i and F_i ($i = 1, \dots, 6$)]. (d) Comparison of displacement responses in the x , y , and z directions (measured from markers T_6 and F_6) of the cell at the free end; the inset shows an enlarged view of the displacement-time histories in the y and z directions.

($i = 0, \dots, 2N$), with $i = 0$ referring to the fixed end and $i = 2N$ referring to the free end; the second number j ($j = 1, \dots, 4$) indicates the vertices at the connection between the i th and $(i + 1)$ -th cells, arranged in a counterclockwise direction. As an example, Fig. 5(a) shows the vertex numbers in two adjacent SMO cells (i.e., four half-cells). In what follows, such a numbering scheme is used, including in the subscripts.

Based on the observations we obtained from the preliminary experiment, four assumptions are made for dynamic modeling purposes.

Assumption (1) Rigid facets and ideal creases within each half-cell. Observation (i) indicates that during deployment, folding of the constituent half-cells is still dominated by rigid folding. Hence, when developing the dynamic model, the origami facets are assumed to be rigid, and the creases within each half-cell are assumed to be ideal hinges [denoted by solid lines in Fig. 5(a)]. With this assumption, the rigid-folding kinematics of each half-cell can be strictly followed in the developed dynamic model.

Assumption (2) Nonideal creases between adjacent half-cells and additional elastic potential energies. The creases shared by adjacent half-cells are not ideal [denoted by dashed lines in Fig. 5(a)], so that the folding motions

of adjacent half-cells can deviate. Nevertheless, their foldings are not fully independent either; they still suffer from strong constraints from the nonideal creases. Specifically, with the nonideal creases, the kinematic constraints between adjacent half-cells are replaced by finite elastic potential energies. An elastic stiffness, k^* , is additionally introduced to the shared creases to constrain the folding deviations between adjacent half-cells. Its contribution to the dynamic model is introduced in detail in Sec. III B 2.

Assumption (3) Boundary conditions. As introduced in Fig. 3(c), at the fixed end, vertex $0,1$ is fully constrained in all three directions (i.e., $x_{0,1} = y_{0,1} = z_{0,1} = 0$); vertex $0,3$ is allowed only to translate in the y direction (i.e., $x_{0,3} = z_{0,3} = 0$); vertices $0,2$ and $0,4$ are allowed to translate within the y - o - z plane (i.e., $x_{0,2} = 0$ and $x_{0,4} = 0$). At the free end of the tube, all vertices are free to move within the space.

Assumption (4) Partial displacement continuity. Displacements are continuous at the vertices $i,1$ ($i = 1, \dots, 2N - 1$) in all three directions. However, the displacement continuity conditions at vertices $i,2$, $i,3$, and $i,4$ are not fully satisfied due to possible deformations of the shared creases between adjacent half-cells. At vertex $i,3$, displacements are continuous in both the x and z directions. At vertices $i,2$ and $i,4$, displacements are continuous only in the x direction.

Based on Assumptions (1), (3), and (4), displacements of the tube in the z direction will be restrained, while displacements in the y direction are admissible, which agree with the observation from preliminary experiments that the vibration in the z direction is much weaker than that in the y direction. Moreover, for a fixed value of i ($i = 0, \dots, 2N$), the vertices i,j ($j = 1, \dots, 4$) are restricted on a plane parallel to the y - o - z plane. Based on Assumption (2), to describe the dynamics of the tube, the DOF has to be increased to the number of constituent half-cells (i.e., $2N$).

B. Dynamic modeling

To describe the dynamics of the Miura-ori tube consisting of $2N$ half-cells, $2N$ generalized coordinates are needed, which are prescribed as the folding angles of the half-cells, i.e., $\boldsymbol{\theta} = (\theta_{1,A}, \theta_{2,A}, \dots, \theta_{2N,A})^T$ [see examples in Fig. 5(a)]. Based on the above assumptions, the governing equations of the tube can be constructed via the Lagrange equation for the general case

$$\frac{d}{dt} \left(\frac{\partial(T - V)}{\partial \dot{\theta}_{i,A}} \right) - \frac{\partial(T - V)}{\partial \theta_{i,A}} = Q_i, \quad (7)$$

where T and V denote the kinetic and potential energies of the tube, respectively; Q_i denotes the nonconservative generalized force associated with the generalized coordinate θ_i .

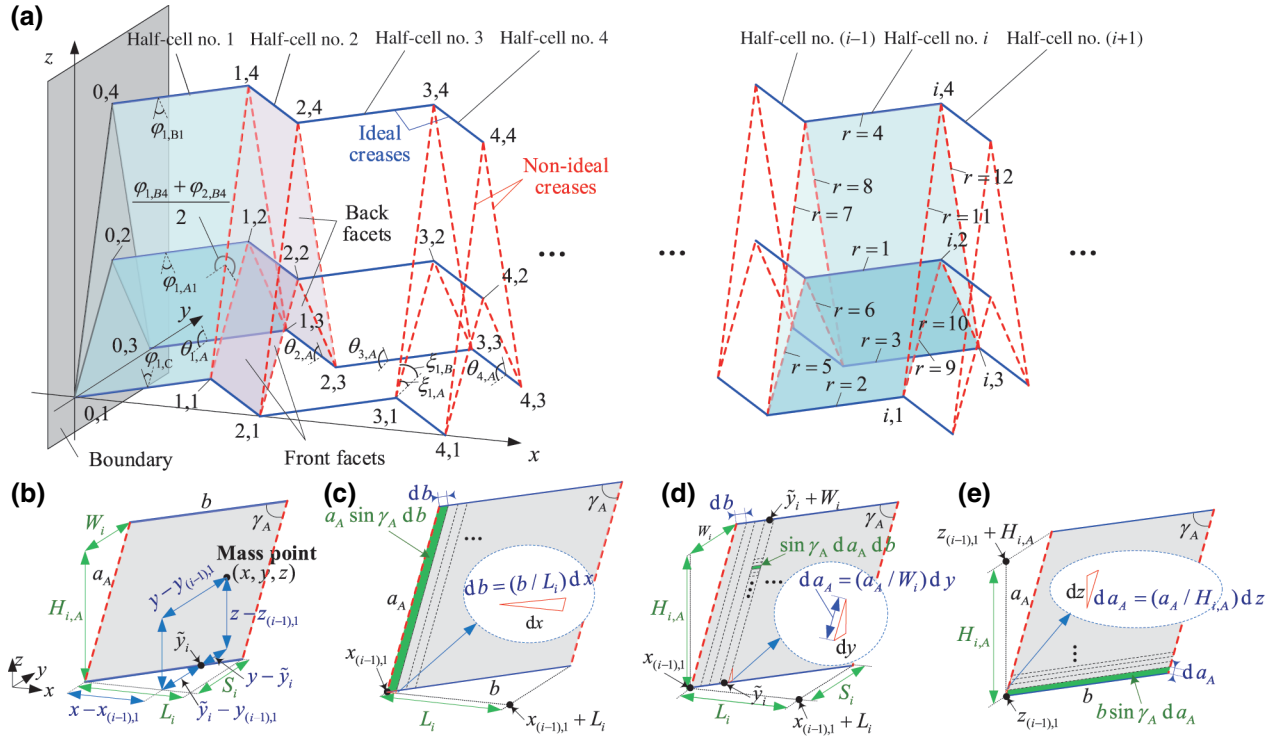


FIG. 5. Illustration of dynamic modeling process. (a) Part of the tube, which consists of seven half-cells, namely, half-cells no. 1 to no. 4 and half-cells no. $(i-1)$, no. i , and no. $(i+1)$. Ideal creases within each half-cell are denoted by solid lines, and nonideal creases shared by adjacent half-cells are denoted by dashed lines. Some angles used for modeling are exemplified, and crease sequence numbers r ($r = 1, \dots, 12$) in the i th half-cell are denoted. (b) As an example, a mass point located on a facet of the i th half-cell is indicated. Dimensions used for expressing the speeds of the mass point are denoted. (c)–(f) Surface integrations performed in the x , y , and z directions, respectively.

1. Kinetic energy

The total kinetic energy, T , of the tube can be expressed as the sum of the kinetic energies of the constituent half-cells, i.e.,

$$T = \sum_{i=1}^{2N} T_i. \quad (8)$$

The kinetic energy of the i th half-cell, T_i , can be further expressed as the sum of the kinetic energies in the x , y , and z directions,

$$T_i = \sum_{k=A,B} \sum_{s=x,y,z} T_{i,ks}. \quad (9)$$

For $T_{i,ks}$, the subscript i ($i = 1, \dots, 2N$) denotes the i th half-cell, k ($k = A, B$) denotes bottom sheet A or top sheet B , and s ($s = x, y, z$) denotes the direction.

Due to the intrinsic reflection symmetry of the half-cell, the velocities of the mass points on the front and back facets are identical in the x and z directions, but are different in the y direction. For the mass point located on the front and back facets [Fig. 5(a)], the velocity in the y

direction is denoted by $v_{i,ky}$ and $v'_{i,ky}$, respectively. By considering the geometric relations [Fig. 5(b)], the velocities of a mass point [with coordinate (x, y, z)] on the facet of the i th half-cell can be determined, which yields

$$\begin{aligned} v_{i,kx} &= \dot{x}_{(i-1),1} + \frac{x - x_{(i-1),1}}{L_i} \dot{L}_i, \\ v_{i,ky} &= \dot{y}_{(i-1),1} + \frac{x - x_{(i-1),1}}{L_i} \dot{S}_i + \frac{y - \tilde{y}_i}{W_i} \dot{W}_i, \\ v'_{i,ky} &= [\dot{y}_{(i-1),1} + \dot{W}_i] + \frac{x - x_{(i-1),1}}{L_i} \dot{S}_i + \frac{y - (\tilde{y}_i + W_i)}{W_i} \dot{W}_i, \\ v_{i,kz} &= \dot{z}_{(i-1),1} + \frac{z - z_{(i-1),1}}{H_{i,k}} \dot{H}_{i,k}, \end{aligned} \quad (10)$$

where $\tilde{y}_i = y_{(i-1),1} + S_i(x - x_{(i-1),1})/L_i$. In Eq. (10), s_{ij} ($s = x, y, z$; $i = 1, \dots, 2N$; $j = 1, \dots, 4$) denotes the absolute position of the vertex ij in the i th half-cell; $v_{i,ks}$ ($i = 1, \dots, 2N$; $k = A, B$; $s = x, y, z$) denotes the velocity of a mass point on the facet of the bottom sheet ($k = A$) or the top sheet ($k = B$) of the i th half-cell in the x , y , or z directions. L_i , W_i , $H_{i,k}$, and S_i are the external dimensions of the i th half-cell given in Eq. (5).

Denoting the areal density of the facet by ρ , the kinetic energy $T_{i,ks}$ can be derived via areal integral. Figures 5(c)–5(e) exemplify how the surface integrations are performed in the three directions.

$$\begin{aligned} T_{i,kx} &= 2\frac{1}{2} \int_{x_{(i-1),1}}^{x_{(i-1),1}+L_i} \rho \left(\frac{a_k b \sin \gamma_k}{L_i} \right) v_{i,kx}^2 dx, \\ T_{i,ky} &= \frac{1}{2} \int_{x_{(i-1),1}}^{x_{(i-1),1}+L_i} \rho \left(\frac{a_k b \sin \gamma_k}{L_i W_i} \right) \\ &\quad \times \left[\int_{\tilde{y}_i}^{\tilde{y}_i+W_i} v_{i,ky}^2 dy + \int_{\tilde{y}_i+W_i}^{\tilde{y}_i+2W_i} (v'_{i,ky})^2 dy \right] dx, \\ T_{i,kz} &= 2\frac{1}{2} \int_{z_{(i-1),1}}^{z_{(i-1),1}+H_{i,k}} \rho \left(\frac{a_k b \sin \gamma_k}{H_{i,k}} \right) v_{i,kz}^2 dz. \end{aligned} \quad (11)$$

After integration, they yield

$$\begin{aligned} T_{i,kx} &= \rho a_k b \sin \gamma_k \left[\frac{1}{3} \dot{L}_i^2 + \dot{x}_{(i-1),1}^2 + \dot{L}_i \dot{x}_{(i-1),1} \right], \\ T_{i,ky} &= \rho a_k b \sin \gamma_k \left[\frac{1}{3} \dot{S}_i^2 + \frac{4}{3} \dot{W}_i^2 + \dot{y}_{(i-1),1}^2 + 2\dot{W}_i \dot{y}_{(i-1),1} \right. \\ &\quad \left. + \dot{S}_i \dot{y}_{(i-1),1} + \dot{W}_i \dot{S}_i \right], \\ T_{i,kz} &= \rho a_k b \sin \gamma_k \left[\frac{1}{3} \dot{H}_{i,k}^2 + \dot{z}_{(i-1),1}^2 + \dot{H}_{i,k} \dot{z}_{(i-1),1} \right]. \end{aligned} \quad (12)$$

Substituting Eq. (12) into Eqs. (8) and (9), the total kinetic energy, T , of the tube can be obtained.

2. Potential energy

The total potential energy, V , of the tube has three origins: the potential energy from the ideal hingelike creases (of length b) within each half-cell V_b , the potential energy from the shared creases between adjacent half-cells V_S , and the potential energy due to the additionally introduced stiffness k^* at the shared creases V_θ , i.e.,

$$V = V_b + V_S + V_\theta. \quad (13)$$

Generally, the creases of the tube are assigned with certain torsional stiffness. For the ideal hingelike creases within each half-cell, the torsional stiffness per unit length is k [Fig. 5(a)]. Hence, the potential energy V_b can be derived as

$$\begin{aligned} V_b &= \sum_{i=1}^{2N} \frac{1}{2} kb [(\varphi_{i,A1} - \varphi_{i,A1}^0)^2 + (\varphi_{i,B1} - \varphi_{i,B1}^0)^2 \\ &\quad + 2(\varphi_{i,C} - \varphi_{i,C}^0)^2], \end{aligned} \quad (14)$$

where the angle $\varphi_{i,k1}$ ($i = 1, \dots, 2N$; $k = A, B$) denotes the dihedral angle between the two adjacent facets of the bottom or top sheets in the i th half-cell, and the angle $\varphi_{i,C}$ denotes the dihedral angle at the connecting creases between the top and bottom sheets in the i th half-cell [see examples in Fig. 5(a)]. They can be analytically obtained by substituting θ_k with $\theta_{i,k}$ in Eqs. (3) and (4). The superscript 0 represents the angle at the stress-free configuration with θ_A^0 .

For the creases that are shared by adjacent half-cells in the bottom sheet and the top sheet, the torsional stiffness per unit length is k and μk , respectively [Fig. 5(a)]. The constant $\mu > 1$ characterizes the stiffness difference. In our experimental prototype, this difference is induced by the embedded prebent spring-steel belts. Corresponding to the shared creases between the $(i-1)$ th and the i th half-cells, the dihedral angles can be expressed as $(\varphi_{(i-1),k2} + \varphi_{i,k2})/2$ and $(\varphi_{(i-1),k4} + \varphi_{i,k4})/2$, where $\varphi_{i,k2}$ and $\varphi_{i,k4}$ ($k = A, B$) can be obtained by substituting θ_k with $\theta_{i,k}$ in Eq. (3) [see an example in Fig. 5(a)]. The potential energy V_S , therefore, includes two parts, namely, the energies from the shared creases in bottom sheet A (V_{SA}) and top sheet B (V_{SB}). Considering that $\varphi_{i,k4} = 2\pi - \varphi_{i,k2}$ always holds, we have

$$\begin{aligned} V_S &= V_{SA} + V_{SB}, \\ V_{SA} &= 2 \sum_{i=1}^{2N-1} \frac{1}{2} ka_A \left[\frac{\varphi_{i,A2} + \varphi_{(i+1),A2}}{2} - \frac{\varphi_{i,A2}^0 + \varphi_{(i+1),A2}^0}{2} \right]^2, \\ V_{SB} &= 2 \sum_{i=1}^{2N-1} \frac{1}{2} \mu ka_B \left[\frac{\varphi_{i,B2} + \varphi_{(i+1),B2}}{2} - \frac{\varphi_{i,B2}^0 + \varphi_{(i+1),B2}^0}{2} \right]^2. \end{aligned} \quad (15)$$

Based on Assumption (2), the folding deviations between adjacent half-cells are constrained by the additional stiffness k^* , which applies to the angular deviations of the shared creases, i.e.,

$$V_\theta = 2 \sum_{i=1}^{2N-1} \frac{1}{2} k^* \{ [\xi_{i,A} - \xi_{(i+1),A}]^2 + [\xi_{i,B} - \xi_{(i+1),B}]^2 \}. \quad (16)$$

Here, $\xi_{i,k}$ ($i = 1, \dots, 2N$; $k = A, B$) is defined as the angle between the crease and the x - o - y plane [see an example in Fig. 5(a)], which has the form

$$\begin{aligned} \cos \xi_{i,A} &= \sqrt{1 - \sin^2 \gamma_A \sin^2 \theta_{i,A}}, \\ \cos \xi_{i,B} &= \frac{\cos \gamma_B}{\cos \gamma_A} \sqrt{1 - \sin^2 \gamma_A \sin^2 \theta_{i,A}}. \end{aligned} \quad (17)$$

Generally, k^* is much larger than the torsional stiffness of the creases; the larger k^* is, the stronger the constraint. Particularly, if $k^* \rightarrow \infty$, the crease angular deviation is completely prohibited, which makes the shared creases become ideal again and degenerates the system into a SDOF rigid-folding dynamic model. Substituting Eqs. (14)–(16) into

Eq. (13), the total potential energy, V , of the tube can be obtained.

3. Nonconservative generalized force

In addition to providing the torsional stiffness, generally, the creases would also dampen the deploying of the tube. Here, viscous damping is assumed to each crease, the damping coefficient per unit length is c_0 . Based on the principle of virtual work, the nonconservative generalized force associated with the generalized coordinate $\theta_{i,A}$ is

$$Q_i = \sum_{r=1}^{12} \left(-c_0 l_{i,r} \frac{d\psi_{i,r}}{dt} \right) \frac{\partial \psi_{i,r}}{\partial \theta_{i,A}}, \quad (18)$$

where $r = 1, \dots, 12$ indicates the 12 crease lines in the i th half-cell [see notations in Fig. 5(a)], $l_{i,r}$ denotes the length of the r th crease, and $\psi_{i,r}$ is the corresponding dihedral angle. Hence, $c_0 l_{i,r} (d\psi_{i,r}/dt)$ is the viscous damping force associated with the r th crease in the i th half-cell. Detailed derivations of the nonconservative generalized forces are given in Ref. [58].

4. Equation of motion

Substituting the kinetic energy, potential energy, and the generalized forces of the tube into the Lagrange equation [i.e., Eq. (7)] and performing necessary simplification, the equation of motion of the Miura-ori tube can be obtained, which can be expressed as the following matrix form:

$$\mathbf{J}\ddot{\mathbf{\theta}} + \mathbf{C}\dot{\mathbf{\theta}} + \mathbf{G}\dot{\mathbf{\theta}}^2 + \mathbf{F}_V = \mathbf{0}, \quad (19)$$

where $\mathbf{J}\ddot{\mathbf{\theta}}$ represents the inertial forces, $\mathbf{C}\dot{\mathbf{\theta}}$ represents the viscous damping forces, $\mathbf{G}\dot{\mathbf{\theta}}^2$ represents the Coriolis and centrifugal forces, and \mathbf{F}_V is the restoring force vector. The dimensions of the matrices \mathbf{J} , \mathbf{C} , and \mathbf{G} are $2N \times 2N$. Detailed derivations of the equation of motion are given in Ref. [58].

C. Transient dynamic responses: An example

Based on Eq. (19), we are then able to analyze the transient dynamics of the tube during free deployment. Here, we first examine an example to demonstrate the effectiveness of the model. Specifically, a six-cell (i.e., $N = 6$) Miura-ori tube (in the nested-in configuration) is studied. The geometric parameters of the tube are the same as those of the prototype (listed in Table I), and the physical parameters are listed in Table II. The tube is first precompressed to an initial configuration, where all constituent half-cells share the same folding angle, i.e., $\theta_{i,A} = \theta_{\text{initial}}$ ($i = 1, \dots, 12$). Then, the precompressed tube is released, and the transient deploying dynamics is obtained by numerically solving Eq. (19) via the fourth-order Runge-Kutta

TABLE II. Physical parameters of the Miura-ori tube.

Parameter	Value	Parameter	Value
k	20 mN/rad	ρ	1.95×10^{-6} kg/mm ²
μ	10	θ_A^0	60°
k^*	4.0×10^5 (mN mm)/rad	θ_{initial}	86.4°
c_0	5 kg/(s rad)		

method. Vibrations of the constituent SMO cells can be characterized by vertices $2i, 1$ ($i = 1, \dots, 6$), because displacements on vertices $2i, 1$ ($i = 1, \dots, 6$) are continuous in all directions [based on Assumption (4)].

Figures 6(a) and 6(b) demonstrate the displacement-time histories of the vertices $2i, 1$ ($i = 1, \dots, 6$) in the x and y directions, respectively, which are qualitatively compared with the experimental results given in Figs. 4(a) and 4(b). Figure 6 reveals that the tube exhibits significant vibrations in both the deploying x direction and the transverse y direction, which agree with the experiments, and meanwhile, fully reflect the effects of relaxing the kinematic constraints and increasing the DOFs. In addition, vibrations at the examined vertices $2i, 1$ are largely synchronized in the overall trend; in both the x and y directions, they exhibit the characteristics of underdamped vibrations, which is consistent with experiments. However, the displacement amplitudes at the examined vertices are different. The vertex $12, 1$ at the free end vibrates with the largest amplitude, which also agrees with the experimental observations. Hence, in what follows, the vertex $2N, 1$ (within the half-cell at the free end) will serve as the representative of the transient dynamics. For this example, the displacement-time histories of the vertex $12, 1$ are extracted and displayed in Figs. 6(c) and 6(d).

Notably, due to the unknown physical parameters of the prototype, a quantitative comparison of the theoretical and experimental results is not performed in this research. However, it is worth noting that a quantitative comparison is important and necessary when implementing the origami tube in practice. To this end, parameter identification and model calibration become prerequisites, which can be done through both model-based and model-free techniques. These constitute our future research directions.

To quantify the transient dynamic performance of the tube, two indexes are examined in this research: the overshoot value and the settling time of vertex $12, 1$ [Figs. 6(c) and 6(d)]. The overshoot value refers to the maximum value that exceeds its final steady-state value, which can be either positive or negative; the settling time is defined as the time required for the output to reach and remain within a given error band. Here, the error bands are prescribed as ± 2.5 mm in the deploying x direction and ± 0.5 mm in the transverse y direction.

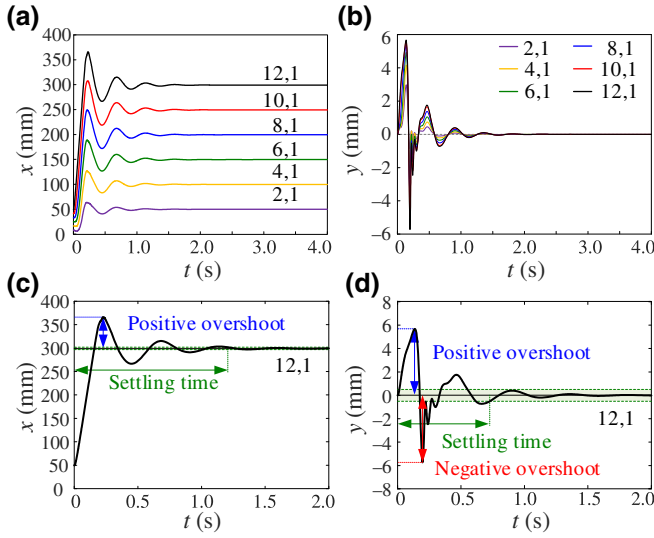


FIG. 6. Free-deployment transient dynamics of a six-cell Miura-ori tube. Displacement-time histories of the vertices $2i, 1$ ($i = 1, \dots, 6$) in the deploying (a) x direction and (b) the transverse y direction. Displacement-time histories of vertex 12,1 in the (c) x and (d) y directions. Examined indexes, namely, the overshoot values and the settling time, are indicated. Shaded bars indicate the prescribed error bands.

IV. EFFECTS OF PHYSICAL AND GEOMETRIC PARAMETERS ON THE TRANSIENT DYNAMIC PERFORMANCE

In this section, we study how the physical and geometrical parameters affect the transient dynamic performance of the Miura-ori tube under free deployment. To this end, a six-cell ($N = 6$) Miura-ori tube (in the nested-in configuration) is studied. In what follows, without repeating, two key indexes are examined, namely, the settling time ($T_{s,x}$ and $T_{s,y}$ in the x and y directions, respectively) and the overshoot values (\hat{x} in the x direction, \hat{y}_+ and \hat{y}_- in the y direction) of the vertex 12,1. We believe that an in-depth understanding of the parameter dependence relationships could provide useful guidance for the development of origami deployable tubes.

A. Physical parameters

This subsection aims to uncover the relationship between the physical parameters and the transient dynamic performance under free deployment. The adjustable physical parameters are the additional stiffness k^* , the crease stiffness k , the stiffness ratio μ , and the viscous damping coefficient c_0 .

1. Effects of the additional stiffness k^*

The additional stiffness k^* (with the unit mN mm/rad) is used to characterize the perfectness of the creases shared by adjacent half-cells; in other words, k^* characterizes the

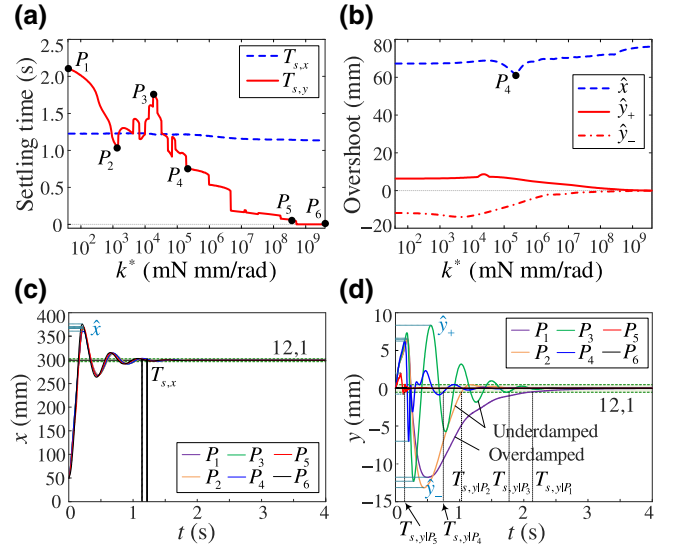


FIG. 7. Effects of additional stiffness k^* on the transient dynamics of the Miura-ori tube under free deployment. (a) Effects on the settling times in the x and y directions. Six points, P_1 to P_6 , are picked out and examined to exemplify the evolution. (b) Effects on the overshoot values in the x and y directions. Displacement-time histories of the vertex 12,1 corresponding to the six points in the (c) x and (d) y directions. Settling times and overshoot values are indicated by dashed lines. Notably, k^* has little effect in the x direction, while in the y direction the effects are significant.

strength of the constraints between adjacent half-cells. The larger the value of k^* is, the more ideal the creases are, and the stronger the constraints applied to the folding deviation between adjacent half-cells. Notably, the value of k^* depends on both the geometric design (width and thickness) and the material of the creases shared by adjacent half-cells. In Ref. [59], such additional stiffness is similarly defined as the pseudojoint stiffness, the magnitude of which is experimentally determined and is on the order of $10^4 - 10^6$ mN mm/rad for polystyrene creases. The creases in our tube prototype are also made of polystyrene films, which indicates that $10^4 - 10^6$ mN mm/rad is a reasonable order of k^* . In this study, to comprehensively study the effects of the additional stiffness, the variable range of k^* is extended bidirectionally by three orders of magnitude to $40, 4 \times 10^9$ mN mm/rad. Figure 7 displays how the settling times and the overshoot values evolve with k^* . The other parameters remain the same as those listed in Tables I and II.

Figure 7(a) reveals that the stiffness k^* has little effect on the settling time in the deploying x direction. By increasing k^* from 40 to 4×10^9 , the settling time $T_{s,x}$ slightly declines from 1.22 to 1.13 s. However, in the transverse y direction, the effect on settling time $T_{s,y}$ is significant. With the increase of k^* from 40 to 4×10^9 , $T_{s,y}$ decreases notably in the overall trend, from 2.10 to 0 s. Specifically, between points P_1 ($k^* = 40$) and P_2 ($k^* = 1786$),

$T_{s,y}$ declines quickly with k^* , following which there is an upturn in $T_{s,y}$ between points P_2 and P_3 ($k^* = 1.78 \times 10^4$). These phenomena can be interpreted in terms of the equivalent damping ratio, if considering vertex 12,1 as a SDOF spring-mass-damper system. When k^* is relatively small, the system is overdamped with an equivalent damping ratio larger than one (e.g., point P_1). With the rise of k^* , the equivalent damping ratio falls off, which significantly diminishes the settling time $T_{s,y}$. At a certain value, the equivalent damping ratio would drop below one, thus switching the system from overdamped (e.g., point P_1) to underdamped (e.g., point P_3) and inducing an elevation of $T_{s,y}$. Further enlarging k^* , although the equivalent damping ratio keeps decreasing, the stiffness k^* becomes large enough to effectively constrain the folding deviations between adjacent half-cells and suppress the transverse vibrations, which, as a result, substantially reduces the settling time $T_{s,y}$ again [e.g., at points P_4 ($k^* = 2.4 \times 10^5$) and P_5 ($k^* = 4 \times 10^8$), $T_{s,y}$ decreases to 0.75 s and 0.15 s, respectively]. At very large values, say, point P_6 with $k^* = 4 \times 10^9$, the settling time converges to zero, indicating that the transverse vibration in the y direction vanishes. This is because the stiffness k^* is sufficiently high to constrain the folding motions of adjacent half-cells and make them consistent. In this case, the MDOF dynamic model degenerates into a SDOF rigid-folding dynamic model. The above analyses are verified via the displacement-time histories of vertex 12,1, corresponding to the six points P_1 to P_6 , as shown in Figs. 7(c) and 7(d).

The stiffness k^* also affects the overshoot values. In the x direction, except for an abrupt drop of \hat{x} at point P_4 , the overshoot value \hat{x} rises slowly with k^* in the overall trend. On the contrary, in the y direction, corresponding to the evolution from the overdamped scenario to the underdamped scenario, the overshoot value $|\hat{y}_-|$ experiences a gentle climb, while \hat{y}_+ remains steady. After that, since the transverse vibrations are effectively suppressed, the overshoot values (\hat{y}_+ and $|\hat{y}_-|$) decline significantly. When $k^* = 4 \times 10^9$, both \hat{y}_+ and \hat{y}_- become zero, suggesting the model degenerates again.

In summary, Fig. 7 suggests that it is necessary to consider the dynamic effects of additional stiffness k^* when designing and modeling origami deployable tubes. Particularly, as a useful equivalence, putting the equivalent damping ratio into consideration could prevent performance deterioration in transverse vibrations. Generally, with a relatively large stiffness k^* (or the stiffness ratio λ), although there is a small growth of the overshoot value in the folding direction, vibrations in the transverse direction can be effectively restrained.

2. Effects of the crease stiffness k and the stiffness ratio μ

The crease stiffness k (with the unit mN/rad) and the stiffness ratio μ are two important parameters that

determine the mechanical properties of the origami tube. Figure 8 displays their effects on the transient dynamics, with k varying from 5 to 50 mN/rad and μ varying from 1 to 50. The other parameters are the same as those listed in Tables I and II.

Figure 8(a) reveals that, in the deploying direction, the settling time $T_{s,x}$ undulates with the increase of k and μ . Overall, $T_{s,x}$ is larger when k or μ take smaller values. Particularly, the peak of $T_{s,x}$ is located in the domain where both k and μ are relatively small. Contrary to expectations, the trough of $T_{s,x}$ does not occur in the domain where both k and μ tend to the maximum; rather, it is located within an arc-shaped stripe where k and μ take moderately large values. Unlike the settling time, the overshoot value \hat{x} monotonically increases with k and μ in the overall trend [Fig. 8(b)]. The peak and bottom are achieved when k and μ reach the maxima and minima, respectively.

In the transverse direction, the trend of the settling time goes into a sharp reverse [Fig. 8(c)]. Overall, the peak of $T_{s,y}$ is reached when k and μ tend to maxima, and the valley of $T_{s,y}$ is located within an arc-shaped stripe where k and μ are relatively small. The overall shoot values (\hat{y}_+ and \hat{y}_-) share the same overall trend with that of \hat{x} , i.e., they monotonically increase with k and μ [Figs. 8(d) and 8(e)]. The trend of \hat{y}_- exhibits better monotonicity than that of \hat{y}_+ .

The above analyses on the effects of k and μ provide useful guidelines for assigning stiffness. On one hand, in terms of the settling time, a compromise is necessary because $T_{s,x}$ and $T_{s,y}$ exhibit opposite trends. For example, at point Q_1 ($\mu = 6$, $k = 6$), the settling time $T_{s,x}(Q_1) = 1.39$ s, which is longer than that at point Q_2 ($\mu = 40$, $k = 40$) with $T_{s,x}(Q_2) = 1.18$ s [Fig. 8(f)]. However, in the y direction, point Q_2 outstrips point Q_1 , with $T_{s,y}(Q_1) = 0.78$ s and $T_{s,y}(Q_2) = 1.09$ s [Fig. 8(g)]. On the other hand, in terms of the overshoot, taking relatively small values of k and μ is always beneficial. For example, the overshoot values (\hat{x} , \hat{y}_+ , and \hat{y}_-) corresponding to point Q_1 are always much lower than those corresponding to point Q_2 [Figs. 8(f) and 8(g)].

In addition to the two indexes, we note that the transient behaviors corresponding to points Q_1 and Q_2 are significantly different in terms of their oscillation frequencies and decaying trends [Figs. 8(f) and 8(g)]. This can be interpreted from the perspective of equivalent stiffness and equivalent damping ratios, if considering the vertex 12,1 as a SDOF spring-mass-damper system. For example, a comparison of the displacement-time histories suggests that the equivalent damping ratios corresponding to point Q_1 in both the x and y directions are much larger than those corresponding to point Q_2 .

It is also worth pointing out that changing the values of k and μ would fundamentally alter the stability characteristics of the tube. As shown in Fig. 8(h), when $\mu > 11.14$, the tube possesses different degrees of bistability, i.e., the tube could stay at either the nested-in or the bulged-out

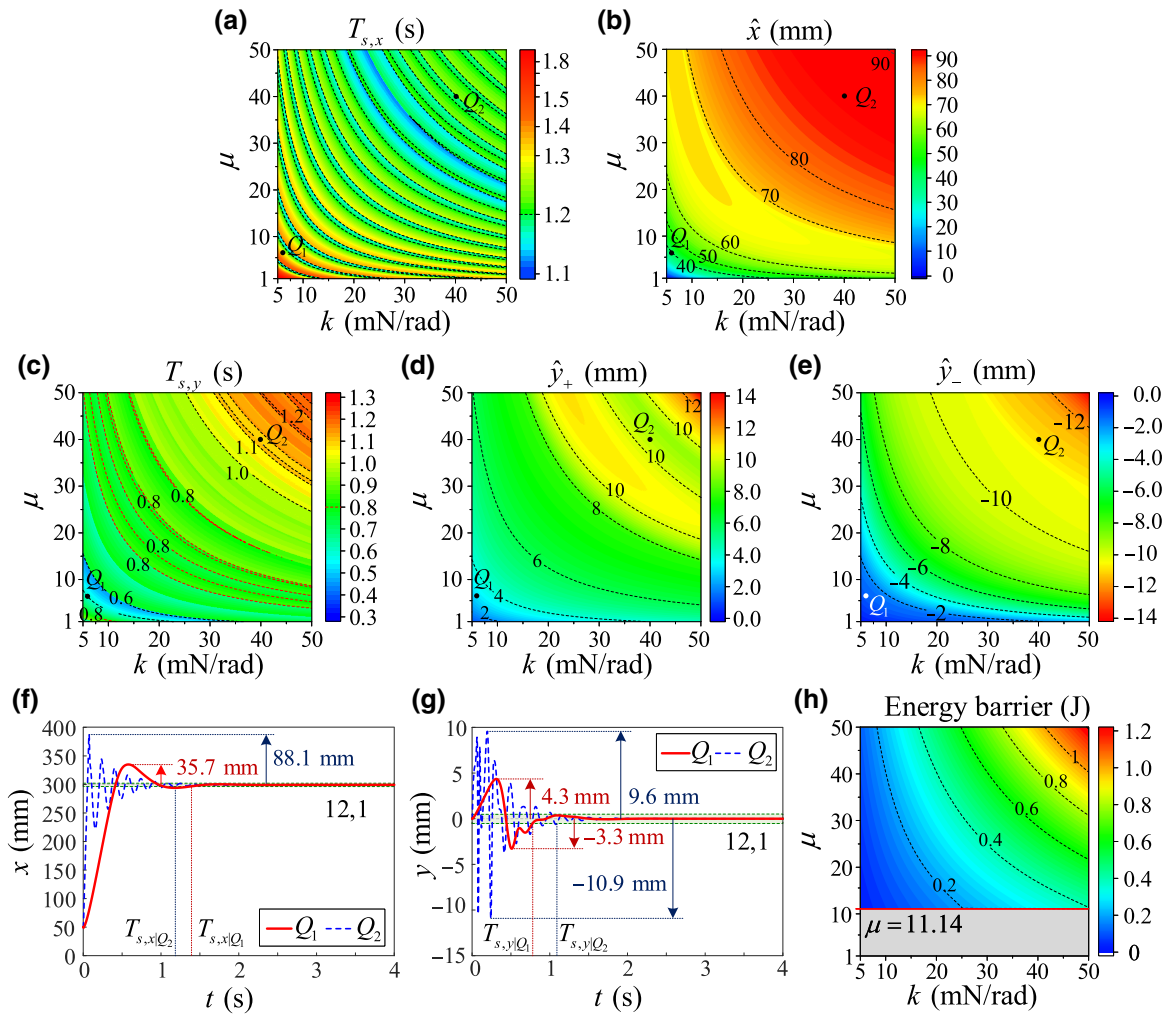


FIG. 8. Effects of stiffness k and ratio μ on the transient dynamics of the Miura-ori tube under free deployment. Effects on (a) the settling time and (b) the overshoot value in the x direction. Effects on (c) the settling time and (e) the overshoot values in the y direction. Two points, Q_1 and Q_2 , are picked out and examined to exemplify evolution. Displacement-time histories of the vertex 12,1 corresponding to the two points in the (f) x and (g) y directions. Settling times and overshoot values are indicated. (h) Effects on the overall stability profile of the tube. Below the critical value $\mu = 11.14$ (shaded), the system is monostable; in the bistable region ($\mu > 11.14$), contours of the energy barrier level are plotted. Energy barrier level is defined as the energy difference between the unstable configuration and the stress-free configuration.

stable configurations, which has pros and cons. On one hand, bistability could endow the tube with the unique capability of fast and accurate configuration switching via external forces, internal pressure, or dynamic excitation; on the other hand, bistability is a global strong nonlinearity that may trigger complex dynamics [46]. When designing origami tubular deployable structures, this issue deserves attention.

3. Effects of the damping coefficient c_0

Figures 9(a) and 9(b) show the effects of the damping coefficient c_0 (with the unit kg mm/s) on the settling times ($T_{s,x}$, $T_{s,y}$) and the overshoot values (\hat{x} , \hat{y}_+ , and \hat{y}_-). The other parameters are the same as those listed in Tables I

and II. In the deploying direction, with the increase of c_0 from one to ten, the settling time $T_{s,x}$ decays sharply to a tiny value; after that, the downward trend becomes gentle, and $T_{s,x}$ reaches the valley of 0.27 s at $c_0 = 23.02$. Such a reduction of $T_{s,x}$ can be attributed to the increase of the equivalent damping ratio, if considering the vertex 12,1 as a SDOF spring-mass-damper system. If c_0 continues to grow, surprisingly, $T_{s,x}$ starts to climb again. We find that the equivalent damping ratio reaches the critical value at point R_3 with $c_0 = 24.92$. After exceeding this value, the system works in the overdamped scenario, and a further increase of the damping ratio would significantly slow the deploying process, thus, enlarging $T_{s,x}$. Particularly, when c_0 takes a very large value, say, $c_0 = 100$, at point R_5 , $T_{s,x}$ is increased to 2.37 s. Figure 9(c) shows the

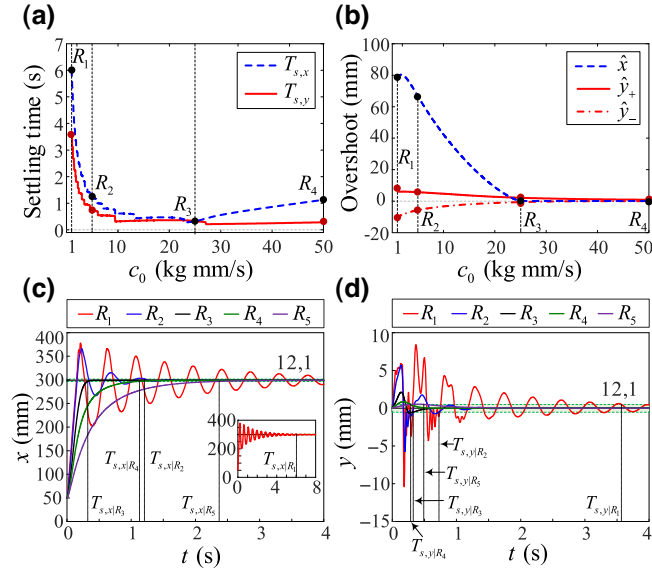


FIG. 9. Effects of damping coefficient c_0 on the transient dynamics of the Miura-ori tube under free deployment. (a) Effects on settling times. (b) Effects on overshoot values. To demonstrate evolution trends, five points are picked out, namely, R_1 ($c_0 = 1$ kg mm/s), R_2 ($c_0 = 5$ kg mm/s), R_3 ($c_0 = 24.92$ kg mm/s), R_4 ($c_0 = 50$ kg mm/s), and R_5 ($c_0 = 100$ kg mm/s). Corresponding displacement-time histories of vertex 12,1 in the (c) x and (d) y directions.

displacement-time histories of vertex 12,1 in the x direction, corresponding to the five characteristic values of c_0 , from which evolution of the system from the underdamped scenario (R_1 and R_2) to the critically damped point (R_3), and to the overdamped scenario (R_4 and R_5), accompanying the abovementioned variation trend of $T_{s,x}$ can be clearly observed.

In the transverse direction, which is similar to that of $T_{s,x}$, the settling time $T_{s,y}$ drops rapidly when c_0 increases from one to ten. However, unlike in the x direction that $T_{s,x}$ stops to increase, $T_{s,y}$ will stabilize at a very low level. Although some small rise is detected, $T_{s,y}$ can no longer gain a large boost, even if c_0 takes a very large value. The variation trend of $T_{s,y}$ can be verified by the displacement-time histories of vertex “12,1” in the y direction, corresponding to the five characteristic values of c_0 (R_1 to R_5), as shown in Fig. 9(d).

The effects of c_0 on the overshoot values are much simpler [Fig. 9(b)]. In both the deploying and transverse directions, the overshoot values (\hat{x} , \hat{y}_+ , and \hat{y}_-) decrease monotonously with the increase of c_0 . Specifically, \hat{x} experiences a significant reduction from 80 to 0 mm by increasing c_0 from 1 to 50. In the transverse direction, although \hat{y}_+ and \hat{y}_- also decrease with c_0 , the reductions are limited, with \hat{y}_+ dropping from 8.4 to 0.85 mm and \hat{y}_- dropping from -10.4 to 0 mm. It can be expected that they will converge to zero, when c_0 takes a very large value.

Figure 9 suggests that an overlarge value of c_0 is not always helpful. To achieve optimum transient performance during free deployment, c_0 should be chosen such that the equivalent damping ratio reaches the critically damped value.

B. Geometric parameters

This subsection studies the effects of the design geometries on the transient dynamics. For the Miura-ori tube, the tailorable geometric factors are the crease length ratio a_A/b , the sector angles γ_k ($k = A, B$), the number of constituent SMO cells N , and the stable configuration.

1. Effects of the crease length ratio a_A/b and the sector angle γ_A

The effects of the geometry parameters on the settling times and the overshoot values are shown in Fig. 10. In detail, the crease length b and the sector angle γ_B are fixed, which are listed in Table I, while the crease length a_A (with unit mm) and the sector angle γ_A (with unit rad) are assumed to be variable ($a_A/b \in [0.5, 2.0]$, $\gamma_A \in [\pi/12, 5\pi/12]$). The physical parameters are the same as those listed in Table II. The scenarios when $\gamma_A \in [0, \pi/12]$ and $\gamma_A \in [5\pi/12, \pi/2]$ are not considered, because, for the former case, the Miura-ori cells would become extremely slender as $\gamma_A \rightarrow 0$ and, for the latter case, the assumption that $a_A < a_B$ would be violated when $\gamma_A > 5\pi/12$.

Figure 10(a) reveals that, in the deploying direction, the settling time $T_{s,x}$ peaks when $\gamma_A = 0.81$ and $a_A/b = 2.0$ and decreases as γ_A tends to the boundaries $\pi/12$ and $5\pi/12$. For the overshoot value \hat{x} , it also takes relatively low values when γ_A tends to the boundaries; the maximum is reached at $\gamma_A = 0.925$ and $a_A/b = 1.36$ [Fig. 10(b)].

In the transverse direction, settling time $T_{s,y}$ shares a similar trend to that of $T_{s,x}$ [Fig. 10(d)], with the maximum being reached at $\gamma_A = 0.84$ and $a_A/b = 2.0$. However, the contours of the overshoot values (\hat{y}_+ and \hat{y}_-) are significantly different from \hat{x} [Figs. 10(e) and 10(f)]. Overall, \hat{y}_+ increases monotonously as γ_A increases; \hat{y}_+ peaks at $\gamma_A = 5\pi/12$ and $a_A/b = 2.0$ and minimizes at $\gamma_A = \pi/12$ and $a_A/b = 0.5$. The overall trend of \hat{y}_- is similar to that of \hat{y}_+ , except that \hat{y}_- reaches a maximum at $\gamma_A = 1.07$ and $a_A/b = 1.64$ and starts to decrease upon further increasing the value of γ_A .

To better understand the above-concluded evolution trends of the settling times and the overshoot values, two points, S_1 ($\gamma_A = 0.92$, $a_A/b = 1.5$) and S_2 ($\gamma_A = 1.3$, $a_A/b = 0.8$), are picked out and examined. The corresponding crease patterns of the Miura-ori cells are sketched in Fig. 10(c), and the displacement-time histories in the x and y directions are displayed in Figs. 10(g) and 10(h), respectively. Obviously, in terms of the settling time, point S_2 behaves better because $T_{s,x|S_2} < T_{s,x|S_1}$ and $T_{s,y|S_2} < T_{s,y|S_1}$. However, in terms of the overshoot values, a design

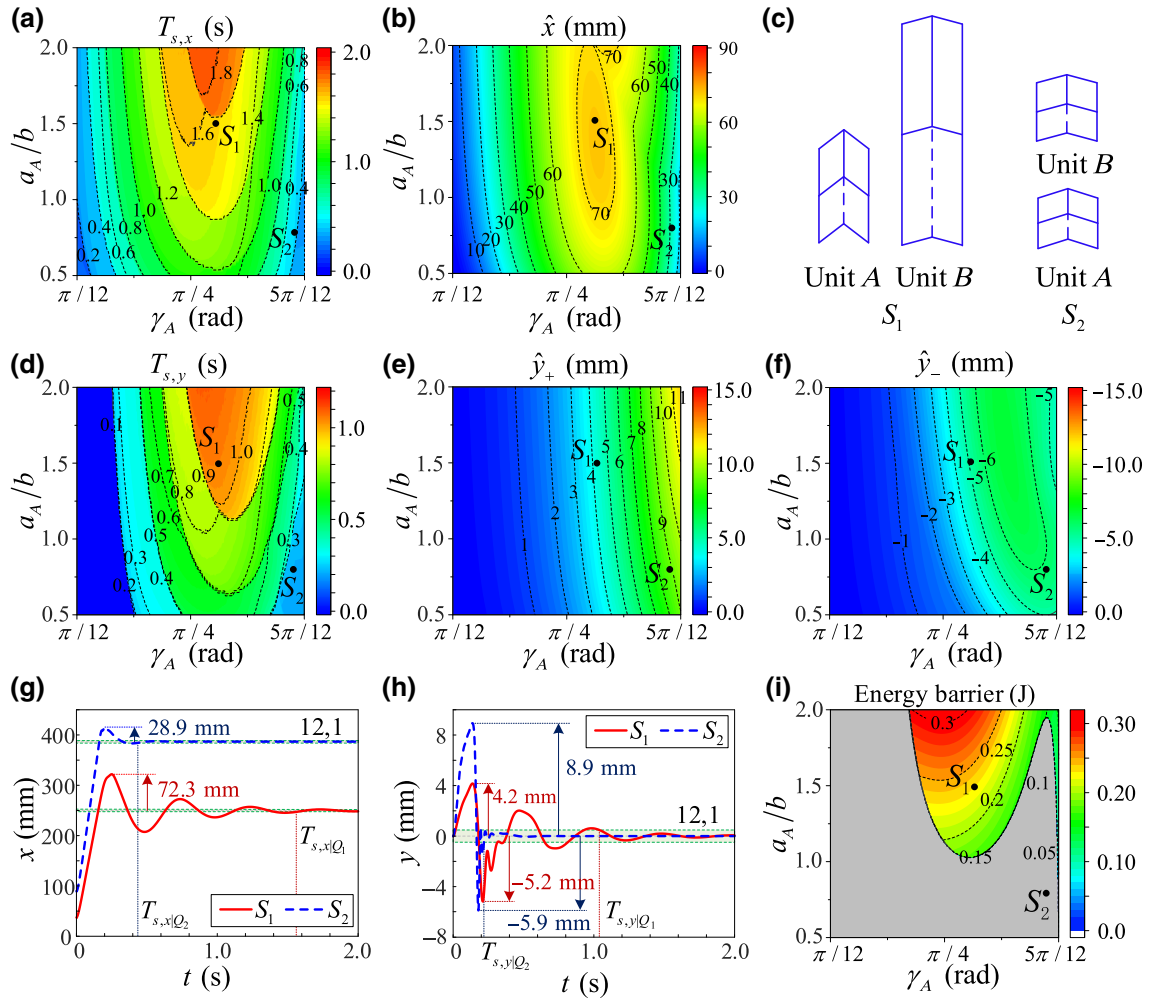


FIG. 10. Effects of the geometric parameters a_A/b and γ_A on the transient dynamics of the Miura-ori tube under free deployment. Effects on (a) the settling time and (b) the overshoot value in the x direction. (d)–(f) Effects on the settling time and the overshoot values in the y direction. Two points, S_1 and S_2 , are picked out to exemplify the evolution; corresponding crease patterns of the Miura-ori cells are sketched in (c). Displacement-time histories of vertex 12,1 corresponding to the two points in the (g) x and (h) y directions. Settling times and overshoot values are indicated. (i) Effects on the overall stability profile of the tube. Monostable region is denoted by shading; in the bistable region, contours of the energy barrier level are plotted.

compromise is needed because $\hat{x}_{S_2} < \hat{x}_{S_1}$, while $\hat{y}_{+|S_2} > \hat{y}_{+|S_1}$ and $\hat{y}_{-|S_2} > \hat{y}_{-|S_1}$. We also remark here that the geometric parameters a_A/b and γ_A would also affect the stability profile. Figure 10(h) shows that both monostable and bistable profiles can be achieved, which needs extra attention during design.

2. Effects of the number of constituent SMO cells N

We also study how the number of constituent SMO cells affects the transient behavior of the tube. With N SMO cells in a tube, the degrees of freedom become $2N$. Figures 11(a) and 11(b) show the effects on the settling times ($T_{s,x}$ and $T_{s,y}$) and the overshoot values (\hat{x} , \hat{y}_+ , and \hat{y}_-), with N varying from one to eight. As expected, both the

settling times and the overshoot values are positively correlated with N . However, it is worth noting that the indexes

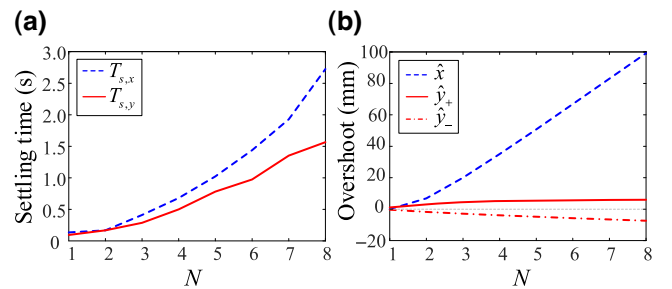


FIG. 11. Effects of the number of constituent cells on the transient dynamics of the Miura-ori tube under free deployment. (a) Settling times. (b) Overshoot values.

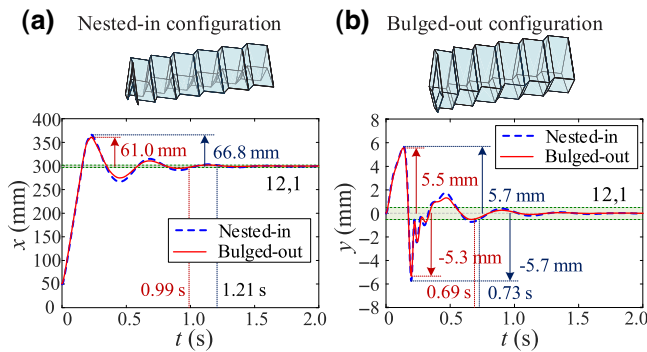


FIG. 12. Displacement-time histories of vertex 12,1 in a nested-in tube and a bulged-out tube under free deployment in (a) the x direction and (b) the y direction. Settling times and overshoot values are indicated.

in the deploying direction are more sensitive to the increase of N , which calls for additional attention in the design.

3. Effects of the stable configurations

Notably, the Miura-ori tube possesses two topologically different configurations, the nested-in and the bulged-out configurations. It is then necessary to comment on whether the transient dynamic performance will have a significant change when the tube switches its stable configuration. To this end, a nested-in tube and a bulged-out tube under free deployment are investigated. For the bulged-out configuration, the stress-free angle is changed to $\theta_A^0 = -60^\circ$, and the initial configuration is changed to $\theta_{\text{initial}} = -86.4^\circ$. The other geometric and physical parameters are the same as those listed in Tables I and II. Corresponding to the two configurations, the displacement-time histories of vertex 12,1 in the x and y directions are displayed in Figs. 12(a) and 12(b), respectively. It reveals that, qualitatively, they make no big difference to the overall trend. Quantitatively, the settling time and the overshoot values corresponding to the nested-in configuration are a little higher than those corresponding to the bulged-out configuration, which can be interpreted in terms of the tangent stiffness [60]. As a result, aiming at different requirements, both configurations are applicable, with small differences in free-deployment performance.

V. SUMMARY AND CONCLUSIONS

With infinite design space, excellent deformability, and extraordinary folding-induced mechanical properties, origami designs have received extensive attention in the development of deployable structures. However, compared with the enormous progress achieved in the areas of crease pattern designs, the packaging techniques, the stowed and deployed configurations, and the quasistatic properties, the dynamics of origami deployable structures, particularly, the transient deploying dynamics is not well understood

due to the lack of a mature modeling methodology. Aiming at advancing the state of the art, this paper investigates the transient dynamic behavior of a Miura-origami tube during free deployment. The reason for choosing the Miura-origami tube as the object of study is that the Miura-origami pattern is a relatively simple geometrical design, and the deployable tubes are characterized by strengths in load carrying and shape transformation.

To tackle the transient dynamics problem, a preliminary free-deployment test is first carried out on a practical Miura-origami tube prototype. It reveals that, in addition to the transient oscillations in the deploying direction, the tube could also exhibit significant transverse vibrations, which are induced by the non-negligible folding deviations between adjacent half-cells. To describe such phenomena, the rigid-folding SDOF dynamic model is no longer adequate. Observations from the experiments provide us with useful guidelines for simplifying dynamic modeling. By admitting the rigid-folding kinematics within each half-cell and replacing the kinematic constraints between adjacent half-cells with additional potential energy, an accurate and processible MDOF dynamic model is developed via first principles. Based on this model, we are then able to predict the transient dynamics of the tube in both the deploying and the transverse directions.

This paper then carries out a comprehensive study to uncover the effects of the physical and geometrical parameters on the transient dynamics, which is characterized by the settling times and the overshoot values in both the deploying and the transverse directions. An interesting finding is that the parametric dependence relationships are sometimes contradictory in the deploying and the transverse directions. For example, enlarging the damping coefficient is generally favorable in suppressing the transverse vibrations; nevertheless, in the deploying direction, an overlarge damping coefficient would significantly increase the settling time for the tube being deployed to the desired configuration. Such a contradiction is also encountered when examining the geometries of the origami tube. In the deploying and transverse directions, the relationships between the overshoot values and the sector angle (γ_A) are opposite in the overall trend. The obtained relationships between the parameters and the transient dynamic behaviors of the tube lay a solid foundation for developing Miura-origami deployable tubes with robust dynamic performance. In particular, the observed contradictions between the deploying and the transverse directions suggest that a compromise in design is sometimes necessary.

We also want to remark here that the underlying philosophies employed in this research, i.e., extracting and abstracting core features of folding from experiments, making reasonable assumptions and simplifications, are general and important. Although only the Miura-origami tube is exemplified, we believe that the proposed dynamic modeling technique could be applied to other origami

structures. This brings up several interesting questions that are worthy of future study. For example, a detailed finite-element model and simulation study would be beneficial to verify the rationality of the dynamic modeling assumptions. Also, if both the facet stiffness and the crease stiffness are low and have the same order of magnitude, all creases can be nonideal and the facets may bend as well. Will such complications significantly change the equivalent dynamic modeling process? That is, can a generic dynamic modeling methodology for origami structures with nonideal creases and facets be developed? Moreover, without accurately obtaining the parameter values, quantitative predictions of the origami dynamics are impossible. Then, how can the geometric and physical parameters of a practical origami structure be determined? Adopting model-based parameter identification might be a feasible way [61].

ACKNOWLEDGMENTS

This research is supported by the National Natural Science Foundation of China under Grants No. 11902078 and No. 11932015, the Major Research Plan of the National Natural Science Foundation of China under Grant no. 91748203, and the Shanghai Rising-Star Program under Grant No. 20QA1400800.

-
- [1] G. E. Fenci and N. G. R. Currie, Deployable structures classification: A review, *Int. J. Sp. Struct.* **32**, 112 (2017).
- [2] G. Kiper and E. Soylemez, in *2009 4th International Conference on Recent Advances in Space Technologies* (IEEE, 2009), pp. 131–138.
- [3] I. Doroftei and I. A. Doroftei, Deployable structures for architectural applications - a short review, *Appl. Mech. Mater.* **658**, 233 (2014).
- [4] M. Runciman, J. Avery, M. Zhao, A. Darzi, and G. P. Mylonas, Deployable, variable stiffness, cable driven robot for minimally invasive surgery, *Front. Robot. AI* **6**, 1 (2020).
- [5] D. S. A. De Focatiis and S. D. Guest, Deployable membranes designed from folding tree leaves, *Philos. Trans. R. Soc. A* **360**, 227 (2002).
- [6] H. Kobayashi, M. Daimaruya, and H. Fujita, in *IUTAM Symposium on Dynamics of Advanced Materials and Smart Structures*, edited by K. Watanabe, F. Ziegler (Springer, Netherlands, 2003), pp. 207–216.
- [7] H. Kobayashi, B. Kresling, and J. F. V. Vincent, The geometry of unfolding tree leaves, *Proc. R. Soc. B Biol. Sci.* **265**, 147 (1998).
- [8] A. Lebé, From folds to structures, a review, *Int. J. Sp. Struct.* **30**, 55 (2015).
- [9] N. Turner, B. Goodwine, and M. Sen, A review of origami applications in mechanical engineering, *Proc. Inst. Mech. Eng. Part C J. Mech. Eng. Sci.* **230**, 2345 (2016).
- [10] M. Schenk, A. D. Viquerat, K. a. Seffen, and S. D. Guest, Review of inflatable booms for deployable space structures: Packing and rigidization, *J. Spacecr. Rockets* **51**, 762 (2014).
- [11] E. A. Peraza-Hernandez, D. J. Hartl, R. J. Malak Jr, and D. C. Lagoudas, Origami-Inspired active structures: A synthesis and review, *Smart Mater. Struct.* **23**, 094001 (2014).
- [12] K. Kuribayashi, K. Tsuchiya, Z. You, D. Tomus, M. Umamoto, T. Ito, and M. Sasaki, Self-deployable origami stent grafts as a biomedical application of Ni-rich TiNi shape memory alloy foil, *Mater. Sci. Eng. A* **419**, 131 (2006).
- [13] H. Fang, Y. Zhang, and K. W. Wang, Origami-based earthworm-like locomotion robots, *Bioinspir. Biomim.* **12**, 065003 (2017).
- [14] S. Felton, M. Tolley, E. Demaine, D. Rus, and R. Wood, A method for building self-folding machines, *Science* **345**, 644 (2014).
- [15] D. Rus and M. T. Tolley, Design, fabrication and control of origami robots, *Nat. Rev. Mater.* **3**, 101 (2018).
- [16] S. Kim, D. Lee, G. Jung, and K. Cho, An origami-inspired, self-locking robotic arm that can be folded flat, *Sci. Robot.* **3**, eaar2915 (2018).
- [17] W. Wang, C. Li, H. Rodrigue, F. Yuan, M.-W. Han, M. Cho, and S.-H. Ahn, Kirigami/origami-based soft deployable reflector for optical beam steering, *Adv. Funct. Mater.* **27**, 1604214 (2017).
- [18] R. L. Harne and D. T. Lynd, Origami acoustics: Using principles of folding structural acoustics for simple and large focusing of sound energy, *Smart Mater. Struct.* **25**, 085031 (2016).
- [19] C. Zou, D. T. Lynd, and R. L. Harne, Acoustic Wave Guiding by Reconfigurable Tessellated Arrays, *Phys. Rev. Appl.* **9**, 014009 (2018).
- [20] N. Cheng, A. N. Rodriguez, and A. B. Koger, in *100th ACSA Annual Meeting Proceedings, Digital Aptitudes* (2012), pp. 250–257.
- [21] J. Cai, a. M. Asce, X. Deng, Y. Xu, and J. Feng, Geometry and motion analysis of origami-based deployable shelter structures, *J. Struct. Eng.* **141**, 06015001 (2015).
- [22] Z. Zhai, Y. Wang, and H. Jiang, Origami-Inspired, on-demand deployable and collapsible mechanical metamaterials with tunable stiffness, *Proc. Natl Acad. Sci.* **115**, 201720171 (2018).
- [23] S. Li, H. Fang, and K.-W. Wang, Recoverable and Programmable Collapse From Folding Pressurized Origami Cellular Solids, *Phys. Rev. Lett.* **117**, 114301 (2016).
- [24] S. Li, H. Fang, S. Sadeghi, P. Bhowad, and K. W. Wang, Architected origami materials: How folding creates sophisticated mechanical properties, *Adv. Mater.* **31**, 1805282 (2019).
- [25] K. Miura, The Institute of Space and Astronautical Science Report No. 618 (1985).
- [26] M. Schenk and S. D. Guest, Geometry of miura-folded metamaterials, *Proc. Natl Acad. Sci.* **110**, 3276 (2013).
- [27] Y. Nishiyama, Miura folding: Applying origami to space exploration, *Int. J. Pure Appl. Math.* **79**, 269 (2012).
- [28] R. Wu, P. C. E. Roberts, C. Soutis, and C. Diver, Heliogyro solar sail with self-regulated centrifugal deployment enabled by an origami-inspired morphing reflector, *Acta Astronaut.* **152**, 242 (2018).
- [29] J. Cai, Z. Ren, Y. Ding, X. Deng, Y. Xu, and J. Feng, Deployment simulation of foldable origami membrane structures, *Aerosp. Sci. Technol.* **67**, 343 (2017).

- [30] T. Chen, O. R. Bilal, R. Lang, C. Daraio, and K. Shea, Autonomous Deployment of a Solar Panel Using Elastic Origami and Distributed Shape-Memory-Polymer Actuators, *Phys. Rev. Appl.* **10**, 1 (2019).
- [31] R. Salazar, S. Murthy, C. Pellazar, and A. Stoica, in *2017 IEEE Aerospace Conference* (IEEE, 2017), pp. 1–7.
- [32] S. A. Zirbel, R. J. Lang, M. W. Thomson, D. A. Sigel, P. E. Walkemeyer, B. P. Trease, S. P. Magleby, and L. L. Howell, Accommodating thickness in origami-based deployable arrays, *J. Mech. Des.* **135**, 111005 (2013).
- [33] K. Senda, S. Ohta, Y. Igarashi, A. Watanabe, T. Hori, H. Ito, H. Tsunoda, and K. Watanabe, in *47th AIAA/ASME/ASCE/AHS/ASC Structures, Structural Dynamics, and Materials Conference* (Reston, Virginia, 2006), Vol. 4, pp. 2595–2612.
- [34] J. Cai, X. Deng, Z. Ya, F. Jiang, and Y. Tu, Bistable behavior of the cylindrical origami structure with kresling pattern, *J. Mech. Des.* **137**, 061406 (2015).
- [35] J. Morgan, S. P. Magleby, and L. L. Howell, An approach to designing origami-adapted aerospace mechanisms, *J. Mech. Des. Trans. ASME* **138**, 052301 (2016).
- [36] S. R. Woodruff and E. T. Filipov, in *Earth and Space 2018*, edited by Ramesh B. Malla, Robert K. Goldberg, and Alaina Dickason Roberts (American Society of Civil Engineers, Reston, VA, 2018), pp. 793–803.
- [37] Z. You and N. Cole, in *47th AIAA/ASME/ASCE/AHS/ASC Structures, Structural Dynamics, and Materials Conference* (American Institute of Aeronautics and Astronautics, Reston, Virginia, 2006), p. AIAA 2006-1685.
- [38] E. T. Filipov, G. H. Paulino, and T. Tachi, Origami tubes with reconfigurable polygonal cross-sections, *Proc. R. Soc. A Math. Phys. Eng. Sci.* **472**, 20150607 (2016).
- [39] S. Pellegrino and S. D. Guest, editors, in *IUTAM-IASS Symposium on Deployable Structures: Theory and Applications* (Springer, Netherlands, 2000).
- [40] M. Mobrem, L. D. Peterson, V. Cormarkovic, and F. Montazersadgh, in *4th AIAA Spacecr. Struct. Conf. 2017*, Vol. 1 (2017).
- [41] B. N. McPherson and J. L. Kauffman, in *AIAA Scitech 2019 Forum* (American Institute of Aeronautics and Astronautics, Reston, Virginia, 2019), p. AIAA 2019–0480.
- [42] S. R. Wu, T. H. Chen, and H. Y. Tsai, A review of actuation force in origami applications, *J. Mech.* **35**, 627 (2019).
- [43] H. Yasuda, Y. Miyazawa, E. G. Charalampidis, C. Chong, P. G. Kevrekidis, and J. Yang, Origami-based impact mitigation via rarefaction solitary wave creation, *Sci. Adv.* **5**, 1 (2019).
- [44] H. Yasuda, C. Chong, E. G. Charalampidis, P. G. Kevrekidis, and J. Yang, Formation of rarefaction waves in origami-based metamaterials, *Phys. Rev. E* **93**, 043004 (2016).
- [45] N. Kidambi and K. W. Wang, Dynamics of kresling origami deployment, *Phys. Rev. E* **101**, 063003 (2020).
- [46] H. Fang, S. Li, H. Ji, and K.-W. Wang, Dynamics of a bistable miura-origami structure, *Phys. Rev. E* **95**, 052211 (2017).
- [47] Q. Zhang, H. Fang, and J. Xu, Programmable stopbands and supratransmission effects in a stacked miura-origami metastructure, *Phys. Rev. E* **101**, 042206 (2020).
- [48] S. Sadeghi and S. Li, Fluidic origami cellular structure with asymmetric quasi-zero stiffness for low-frequency vibration isolation, *Smart Mater. Struct.* **28**, 065006 (2019).
- [49] L. M. Fonseca, G. V. Rodrigues, M. A. Savi, and A. Paiva, Nonlinear dynamics of an origami wheel with shape memory alloy actuators, *Chaos, Solitons & Fractals* **122**, 245 (2019).
- [50] G. V. Rodrigues, L. M. Fonseca, M. A. Savi, and A. Paiva, Nonlinear dynamics of an adaptive origami-stent system, *Int. J. Mech. Sci.* **133**, 303 (2017).
- [51] J. Liu, H. Ou, R. Zeng, J. Zhou, K. Long, G. Wen, and Y. M. Xie, Fabrication, dynamic properties and multi-objective optimization of a metal origami tube with miura sheets, *Thin-Walled Struct.* **144**, 106352 (2019).
- [52] L. Bowen, B. Trease, M. Frecker, and T. Simpson, in *ASME 2016 Conference on Smart Materials, Adaptive Structures and Intelligent Systems, SMASIS 2016* (2016), Vol. 1, pp. SMASIS2016-9172.
- [53] J. A. Fulton and H. Schaub, in *Proceedings of the International Astronautical Congress, IAC*, Vols. 2019-October (2019), pp. 1–11.
- [54] H. Fang, T. Chang, and K.-W. Wang, Magneto-Origami structures: Engineering multi-stability and dynamics via magnetic-elastic coupling, *Smart Mater. Struct.* **29**, 015026 (2020).
- [55] J. Cai, X. Deng, Y. Zhang, J. Feng, and Y. Zhou, Folding behavior of a foldable prismatic mast with kresling origami pattern, *J. Mech. Robot.* **8**, 031004 (2016).
- [56] H. Fang, S. Li, H. Ji, and K. W. Wang, Uncovering the deformation mechanisms of origami metamaterials by introducing generic degree-4 vertices, *Phys. Rev. E* **94**, 043002 (2016).
- [57] S. Li and K. W. Wang, Fluidic origami with embedded pressure dependent multi-stability: A plant inspired innovation, *J. R. Soc. Interface* **12**, 20150639 (2015).
- [58] See the Supplemental Material at <http://link.aps.org/supplemental/10.1103/PhysRevApplied.14.034068> for detailed expressions of the nonconservative generalized force and detailed derivations of the equation of motion.
- [59] C. Liu and S. M. Felton, Transformation Dynamics in Origami, *Phys. Rev. Lett.* **121**, 254101 (2018).
- [60] S. Sengupta and S. Li, Harnessing the anisotropic multi-stability of stacked-origami mechanical metamaterials for effective modulus programming, *J. Intell. Mater. Syst. Struct.* **29**, 2933 (2018).
- [61] Z. Liu, H. Fang, K.-W. Wang, and J. Xu, A parameter identification method for continuous-time nonlinear systems and its realization on a miura-origami structure, *Mech. Syst. Signal Process.* **108**, 369 (2018).